ACS APPLIED MATERIALS & INTERFACES

Research Article

www.acsami.org

Enhanced Electrochemical Performance of Three-Dimensional Ni/Si Nanocable Arrays as a Li-Ion Battery Anode by Nitrogen Doping in the Si Shell

Hao Liu and Quan Li*

Department of Physics, The Chinese University of Hong Kong, Shatin, New Territory, Hong Kong

Supporting Information

ABSTRACT: In the present study, a configuration of three-dimensional Ni core/sputtered Si shell nanocable arrays is proposed to alleviate the severe volumetric change of Si during lithiation/delithiation. In particular, the effects of N doping in the Si shell on the electrochemical performance of the nanocable array electrodes have been investigated. It has been found that reduced interfacial resistance, enhanced effective Li ion diffusion coefficient in the active material, and more stable surface passivating layer are likely to be achieved by N doping, leading to an improvement of the rate performance and cyclability when compared to the undoped nanocable array counterpart.

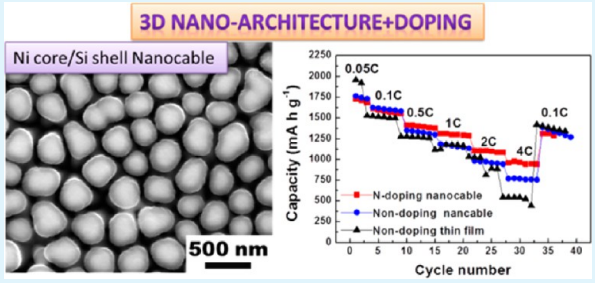

KEYWORDS: *silicon, nanocable, nitrogen doping, Li-ion battery, anode*

INTRODUCTION

The commercial use of Si in lithium cells has been limited by the low cycling stability of bulk Si due to severe volume change during the discharging/charging process and low electrical conductivity of intrinsic Si. To overcome the former problem, nanostructured configurations of Si, e.g., nanoparticles,[1] thin films,[2,3] nanowires,[4,5] and nanotubes,[6,7] are employed to alleviate the volumetric expansion by employing small size to release stress and/or incorporating pores or voids into the corresponding materials. On the other hand, the electrical conductivity of Si is low. Several methods have been explored to enhance the electrical conductivity of Si, such as mixed Si particles with conductive carbon,[8] surface coating with carbon[9] or metal,[10] and doping with other elements.[2,11−13] Among those methods, only doping serves as an intrinsic solution. The doped Si electrode may no longer suffer from detachment between the Si and its surrounding electrical connections.[10] In doping carried out in Si thin films, n-type Si shows better electrochemical performance than that of p-type or intrinsic ones.[2,11] However, most of the reported works about doped Si electrodes were carried out in thin film or particle systems,[2,11,12,14] and limited works focused on three-dimensional (3D) configurations of the nanostructured Si electrode.[15] One work of B-doped porous Si nanowires as a lithium ion battery (LIB) anode exhibited high capacity (~2000 mA h g^{-1} at the rate of ~0.5 C) and high structural stability due to the high porosity and the improved electron conductivity of the doped porous Si nanowires. However, the performance of this kind of anode greatly depends on the proper selection of binders or additives.[15] As the introduction of binders and additives generates undesired interfaces between the active materials and the additives, their presence increases the complexity of the charge transfer process.[16] In the present work, the effect of N doping on the electrochemical performance of Ni core/sputtered Si shell nanocable arrays directly grown on the conductive substrate was investigated as a LIB anode, avoiding the use of binders or additives. In this composited configuration, the metallic Ni nanowire arrays (Ni metal selected due to the good adhesion strength between the Ni metal and sputtering Si[17]) act as both a mechanical support and a nanostructural current collector for the active material Si. In addition, the internal pore of the nanocable array electrode helps to accommodate the large volumetric change during the lithiation/delithiation process, thus mitigating the internal stress built up. Most importantly, N doping is easily realized during the magnetron sputtering process of Si by the introduction of N_2 gas into the sputtering chamber. The N-doped nanocable array electrode exhibits considerable improvement in electrochemical performance when compared to undoped nanocable arrays or a thin film counterpart of the same Si mass.

EXPERIMENT SECTION

Metallic Ni/Si Nanocable Array Growth on a Conductive Substrate. Firstly, the Ni nanowire arrays were directly grown on a Ni foil substrate by electrodeposition with the aid of an anodic alumina oxide (AAO) template, which was described previously.[18] To increase the separation distance between individual Ni nanowires, the sample was electropolished in an acid solution.[18] Then a thin Si layer was

Received: September 27, 2013
Accepted: October 30, 2013
Published: October 30, 2013

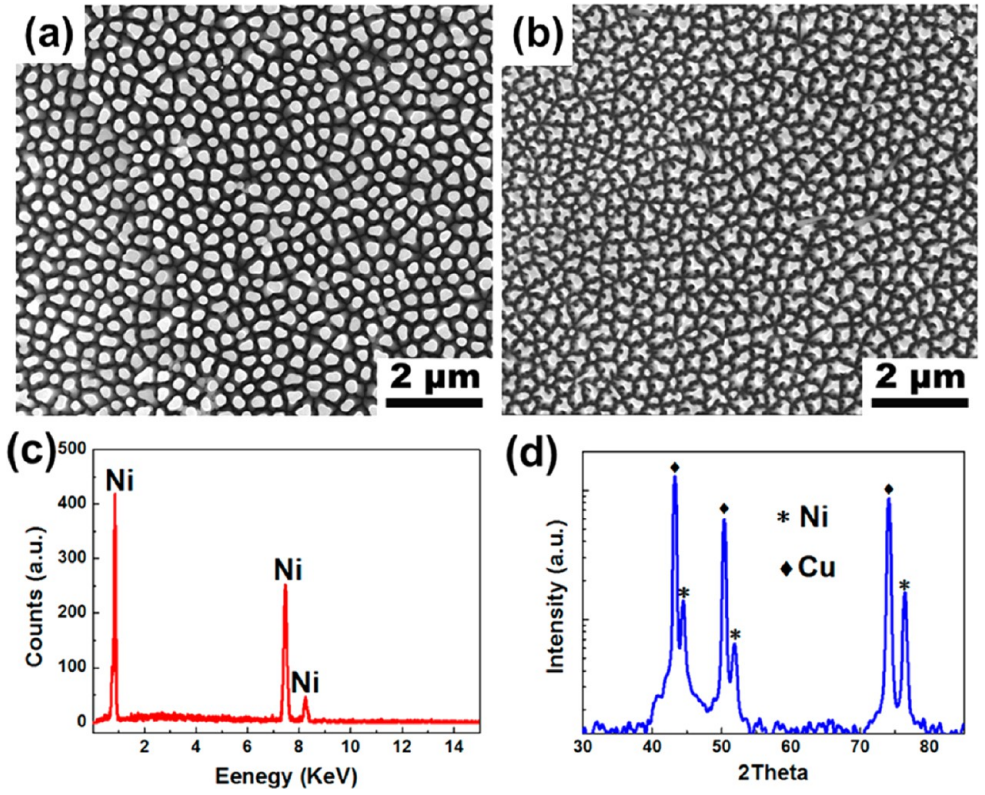

Figure 1. Planview SEM images of the (a) as-depositied and (b) electropolished Ni nanowire arrays. (c) EDX spectrum of the electropolished sample. (d) XRD θ–2θ scan of the electropolished Ni nanowire arrays on a copper substrate.

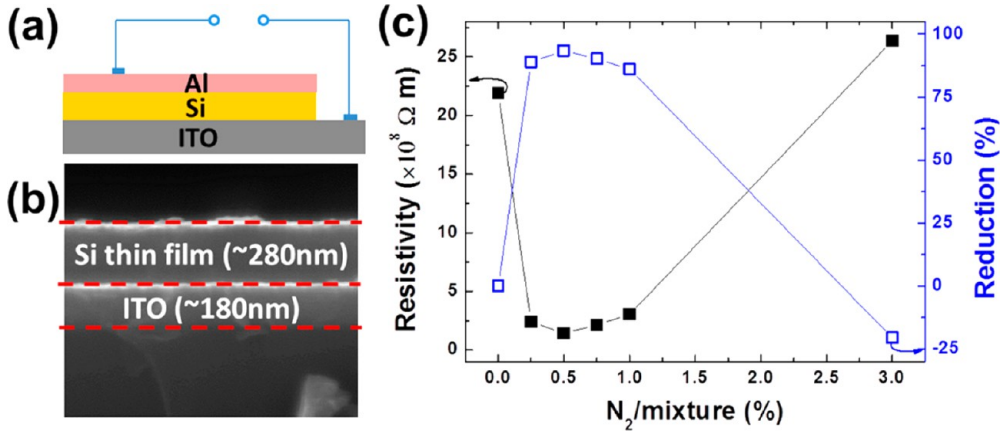

Figure 2. (a) Schematic of resistance measurement of the sputtered Si thin film on ITO. (b) Cross-section SEM image of the sputtered Si on ITO substrate. (c) Relationship between the resistivity of this sample and amount of N_2 gas introduced (in terms of volumetric percentage of the N_2 in the gas mixture).

deposited on the Ni nanowire arrays through radio frequency (RF) magnetron sputtering with a Si target at 100 W. During this process, a chamber pressure kept at 5×10^{-3} Torr with a N_2/Ar mixed gas (volumetric percentage of N_2 in the mixture adjusted from 0% to 3%) flow of 50 standard cubic centimeters per minute (sccm), and the substrate was rotated at 20 rpm to achieve better uniformity.

Characterizations. The crystallinity of the samples was examined by X-ray diffraction (XRD, SmartLab, Rigaku) with a Cu Kα radiation source (d = 0.1541 nm). The morphologies and the chemical composition were characterized by a field emission scanning electron microscope (FESEM, Quanta 200, FEI), equipped with an energy-dispersive X-ray detector (EDX, Oxford). Transmission electron microscopy (TEM) was also carried out for the microstructural investigation of the samples using a Tecnai F20 microscope operating at 200 kV.

Electrochemical Properties of the Metallic Ni/Si Nanocable Array Electrode. The electrochemical properties of the samples were examined using CR2032 coin-type cells with Li foil as counter electrode. No binder or conducting carbon was used during the cell assembly. The liquid electrolyte was 1.0 M $LiPF_6$ in ethylene carbonate/diethyl carbonate solvent (1:1 v/v, Novolyte Co.). All coin cells were cycled between 0.02 and 2.0 V at different rates on a multichannel battery test system (CT2001A, LAND batteries testing system, Wuhan Kingnuo Electronic Co., Ltd.). The electrochemical impedance spectroscopy (EIS) of the batteries was collected in the frequency range from 100 kHz to 1 Hz under an alternating current (AC) stimulus with 10 mV of amplitude (CHI 660C, Shanghai Chenhua Instrument Co., Ltd.). The obtained impedance data were fitted by ZView software. After a cycling test, the coin-cells were disassembled to characterize the morphology change of the electrode.

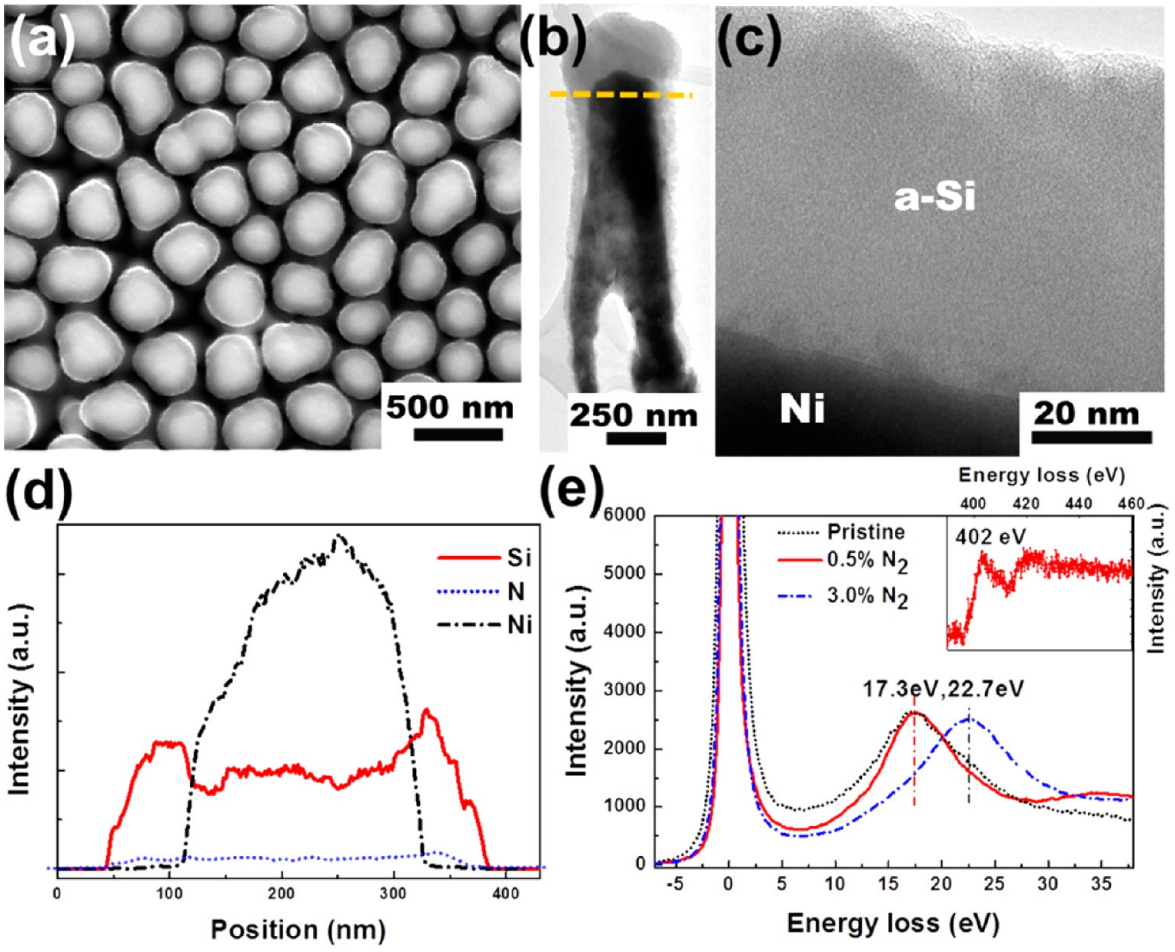

Figure 3. (a) Planveiw SEM images of the sample 0.5% N_2-NC30 min. Typical TEM images taken from the sample 0.5% N_2-NC30 min (b) at low magnification and (c) at higher magnification. (d) EDX line scan taken along the yellow line (in b) from the same nanocable sample. (e) Electron energy loss spectra taken from the Si shell of the sample pristine-NC30 min, sample 0.5% N_2-NC30 min, and sample 3.0% N_2-NC30 min. Electron energy loss spectrum of the N K-edge taken from the Si shell of the sample 0.5% N_2-NC30 min is shown in the inset.

The solid−electrolyte interphase (SEI) layer on the electrode surface was removed by dilute acetic acid.[19]

RESULTS AND DISCUSSION

Figure 1a shows the planview SEM images of as-deposited Ni nanowire arrays. The average diameter and separation distance between individual nanowires are ∼200 nm and ∼130 nm, respectively. They are inherited from the AAO template. The length of the Ni nanowire can be easily controlled in the range of several hundreds of nanometers to several tens of micrometers by changing the electrodeposition duration. In the present work, the Ni nanowire arrays with a length of ∼3 μm have been used as the current collector. To create more space to accommodate active material on the Ni nanowires, the separation distance between the individual nanowires has been increased using electropolishing, the result of which can be seen in Figure 1b. The average diameter of the Ni nanowires is reduced to ∼100 nm, while their separation distance is increased to ∼230 nm. The length of the nanowire is less affected by electropolishing; that is, it remains as ∼3 μm. After removing the AAO template, only the Ni signal is detected in the EDX spectrum (Figure 1c). To determine the crystallinity of the Ni nanowires, a specific sample was grown using Cu foil as the substrate. All XRD peaks come from the Cu (substrate) and Ni (JCPDS No. 4-850) only (Figure 1d).

To find out the correlation between the resistivity of Si and the amount of N dopant, a Si thin film layer was first deposited on an indium tin oxide (ITO) conductive substrate (∼10 Ω/□), before an Al thin layer was sputtered on the surface. This conductive metal electrode also acts as a protective layer to prevent the formation of an insulating SiO_2 layer on the surface of the Si thin film when the sample is exposed to air. The schematic of the Si thin film resistance measurement is shown in Figure 2a. The thickness of Si thin film is ∼280 nm (Figure 2b). The resistivities ρ of the Si thin film can be obtained via the following equation: $\rho = RS/l$, where ρ is the resistivity, R the measurment resistance, S the surface area of the Si thin film, and l the thickness of the Si thin film. Figure 2b shows the relationship between the resistivity of Si thin film and different amounts of N_2 gas introduced (in terms of volumetric percentage of the N_2 in mixed gas). It shows clearly that the resistivity of the Si thin film first decreases (at low level N_2 content doping (0.25−1% in the gas mixture)) then increases when the percentage of N_2 in mixed gas increases from 0% to ∼3%. The Si thin film sample doped in the presence of a 0.5% N_2/gas mixture exhibits the lowest resistivity, showing a 94% reduction when compared to that without doping. Therefore, a 0.5% N_2/gas mixture was used for the doping of Ni/Si nanocable arrays in the later discussions.

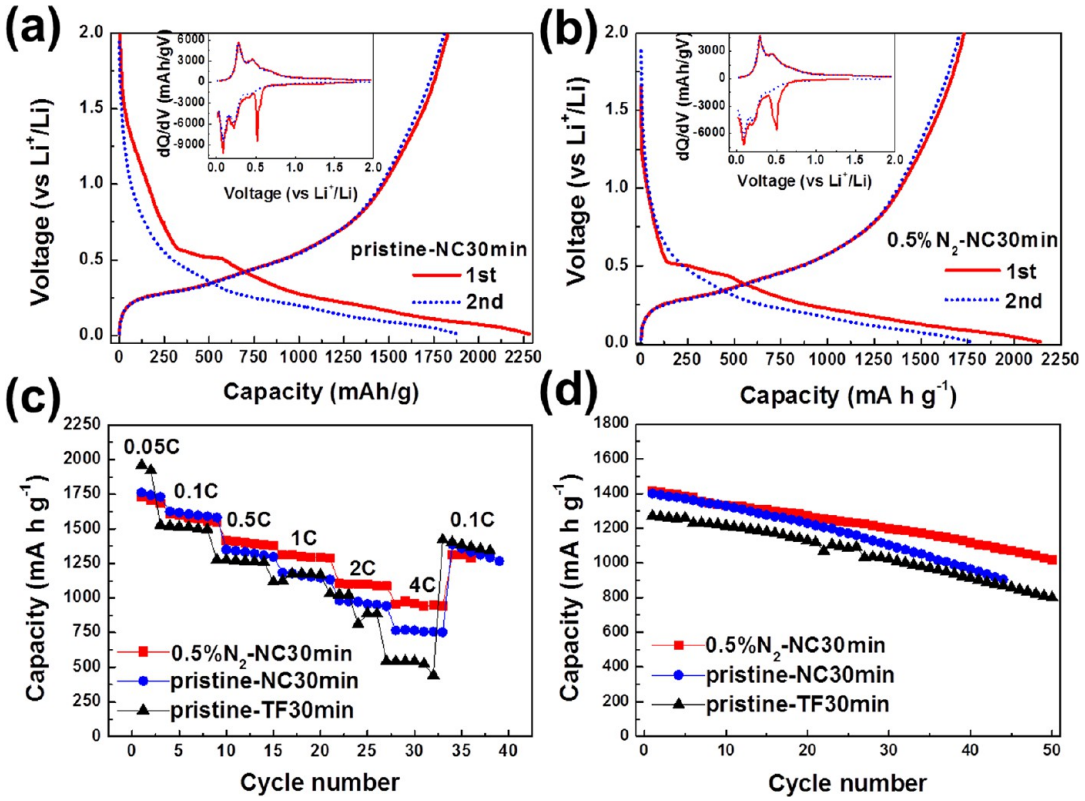

Figure 4. Voltage profiles of the Ni/Si nanocable array electrodes at the first and second cycles under 0.05 C rate. (a) Sample pristine-NC30 min and (b) sample 0.5% N_2-NC30 min. The inset shows their differential capacity–voltage curves. (c) Comparison of charging capacities between the sample pristine-NC30 min, sample 0.5% N_2-NC30 min, and sample pristine-TF30 min at various rates. (d) Capacity of the corresponding samples cycled at a 0.5 C rate.

Figure 3a shows the planview SEM images of the doped Ni/Si nanocable array samples under 0.5% N_2/mixture gas with 30 min sputtering duration (sample 0.5% N_2-NC30 min). The average thickness of the Si shell is estimated at ~58 ± 8 nm. More detailed structural and compositional characterizations of individual nanowires were carried out by TEM related techniques. Figure 3b shows the low-magnified TEM image of a typical individual Ni/Si nanocable taken from the sample 0.5% N_2-NC30 min. The light/dark contrast of the individual wire reveals the core/shell nanocable configuration, although the Si shell on the top of the Ni nanowire is much thicker than that at the side. The formation of the nonconformal Si shell likely results from the shadow effect of the sputtering technique.[20] The shell region appears amorphous in the high-resolution TEM image (Figure 3c), which is consistent with XRD results (not shown). The spatial distribution of the compositional elements of this individual nanocable is disclosed by the EDX line scan (Figure 3d), in which one can see that the Ni and Si locate in the core and shell regions, respectively. The electron energy loss spectra (EELS) taken from sample pristine-NC30 min (undoped nanocable sample with 30 min sputtering duration), sample 0.5% N_2-NC30 min, and sample 3.0% N_2-NC30 min disclose the subtle difference in their electronic structures. Figure 3e shows that the plasmon peak of the Si shell doped under low level N_2 content (e.g., 0.5 % N_2/mixture) is similar to that of pristine Si. The only difference might be the detectable N signal in the 0.5% N_2-NC30 min sample but not in the pristine one (inset of Figure 3e). For a sample doped at higher N_2 level, a shift of the plasmon peak to ~22.7 eV is observed (sample 3.0% N_2-NC30 min), and it is characteristic of Si_3N_4. This result suggests the formation of Si_3N_4 at high N_2 level and is consistent with the increased resistivity of the Si doped at high N_2 level (Figure 2c).

The performance of the sample pristine-NC30 min and sample 0.5% N_2-NC30 min as anode was tested by galvanostatic discharge and charge. The first and second discharging and charging voltage profiles of the two samples under the rate of 0.05 C are shown in Figure 4a and 4b, respectively. Both of them exhibit similar discharging and charging behavior. The differential capacity–voltage curves of those two samples derived from their voltage profiles show a typical discharging and charging behavior of amorphous Si (inset of Figure 4a and 4b). For the sample pristine-NC30 min (inset of Figure 4a), two peaks at ~0.22 and ~0.08 V (vs Li^+/Li) during lithiation and two peaks at ~0.28 and ~0.46 V (vs Li^+/Li) during delithiation are consistent with those of the reported amorphous Si.[21,22] In addition, a peak around 0.50 V in the first discharge relates to the formation of the SEI layer (decomposition of liquid electrolyte). This peak disappears in the second discharging process, indicating most SEI layer is formed at the first discharging process. The differential capacity–voltage curves of the sample 0.5% N_2-NC30 min are similar to those of the sample pristine-NC30 min. However, the lithiation voltage (~0.19 V vs Li^+/Li) is lower than that of the sample pristine-NC30 min, indicating a smaller thermodynamic driving force for lithiation in the N-doped sample. A similar phenomenon also has been observed in the n-type doped crystalline Si anode.[12] In addition, the first discharging and charging capacities of the sample pristine-NC30 min are 2280 and 1826 mA h g^{-1}, slightly higher than that of the sample

dx.doi.org/10.1021/am404258n | ACS Appl. Mater. Interfaces 2013, 5, 12190–12196

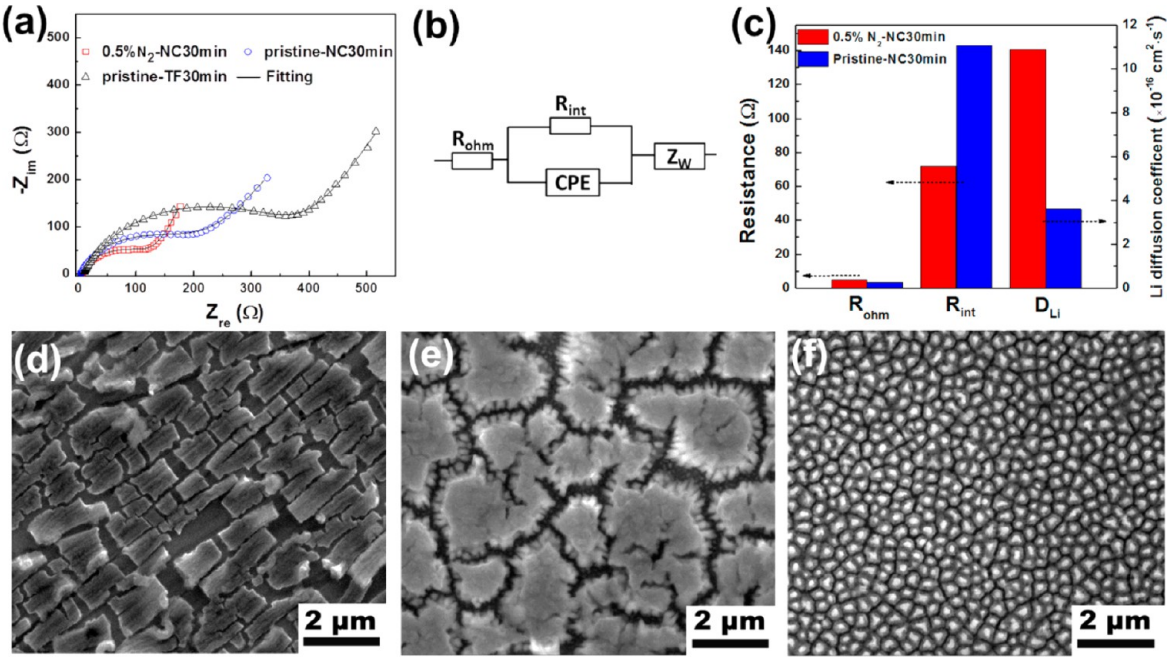

Figure 5. (a) Nyquist plots of the sample pristine-NC30 min, sample 0.5% N_2-NC30 min, and sample pristine-TF30 min at the potential of 2 V vs Li^+/Li during the charging process. (b) The equivalent circuit model for the two electrodes. R_{ohm} stands for series ohmic resistance. R_{int} and CPE represent interfacial reaction resistance and capacitance, respectively. Z_w represents Warburg impedance. The solid lines in (a) are the fitted curves by using this model. (c) Comparison of the individual real impedances, R_{ohm}, R_{int}, and the effective Li diffusion coefficient D_{Li} between those two nanocable electrodes. Planview SEM images of the (d) sample pristine-TF30 min; (e) sample pristine-NC30 min; and (f) sample 0.5% N_2-NC30 min electrodes taken at delithiated states after 30 cycles.

0.5% N_2-NC30 min (2138 and 1731 mA h g^{-1}). Both of the irreversible capacities in the first cycle are around 20%, contributed by the irreversible reaction during the formation of the SEI layer, which is commonly observed on the LIB anode.[23,24]

Figure 4c shows the comparison of charging (delithiation) capacities among the sample pristine-NC30 min, sample 0.5% N_2-NC30 min, and sample pristine-TF30 min (undoped Si thin film (TF) with 30 min sputtering duration, thickness ~140 nm) at various rates. At low rate of 0.05 C, the sample pristine-NC30 min and sample 0.5% N_2-NC30 min exhibit similar charging capacity of ~1750 mA h g^{-1}, while the sample pristine-TF30 min delivers slightly higher capacities of ~1950 mA h g^{-1}. However, the sample 0.5% N_2-NC30 min shows improved capacity retention ability compared to those of the other two, especially at higher charging rate. For example, at high rate of 4 C (~17 A/g), the sample pristine-TF30 min electrode only exhibits charging capacities of ~542 mA h g^{-1}, whereas the sample pristine-NC30 min shows ~766 mA h g^{-1}. Sample 0.5% N_2-NC30 min achieves the highest charging capacity of ~976 mA h g^{-1}. Those results indicate that the rate performance of the sputtered Si electrode can be improved not only by employing a 3D Ni/Si nanocable array configuration but also by N doping. In addition, the cycling stability of the N-doped nanocable array electrode is also increased when compared to those of the other two electrodes. For example, the sample 0.5% N_2-NC30 min cycled at a 0.5 C rate exhibits ~72% charging capacity retention after 50 cycles, which is higher than those of the sample pristine-NC30 min (~65% after 45 cycles) and the sample pristine-TF30 min (~62% after 50 cycles), as shown in Figure 4d.

Figure 5a shows the electrochemical impedance spectra (EIS) of the sample pristine-NC30 min, sample 0.5% N_2-NC30 min, and sample pristine-TF30 min at the potential of 2 V vs Li^+/Li during the charging process. All the spectra have similar features: a depressed semicircle at the high-to-medium frequency region, which represents the interfacial resistance, and a following inclined line at the low frequency region which relates to the diffusion of Li in the solid electrode. The interfacial resistance, which originates from the charge transfer resistance at the interface and the presence of the passivating SEI layer, can be directly determined from the semicircle diameter in the Nyquist plot.[25] An appropriate equivalent circuit model (Figure 5b) is established to fit the Nyquist curves. The fitted results suggest that the interfacial resistances of the sample 0.5% N_2-NC30 min, sample pristine-NC30 min, and sample pristine-TF30 min are 72, 143, and 352 Ω (Table S1, Supporting Information). The smaller interfacial resistance of the nanocable samples (compared to the thin film sample) benefits from its nanostructured configuration, which has higher surface area-to-volume ratio, allowing more absorption and insertion sites for Li ions.[26] Moreover, the carrier transport pathways are also shorter in the nanocable configuration, improving the rate capabilities of the material during the charging/discharging process. On the other hand, the interfacial reaction resistance is further reduced in the sample 0.5% N_2-NC30 min due to the improved electrical conductivity of Si upon doping (Figure 5c). To inspect whether the behavior of Li ion diffusion in the nanocable electrode is affected by doping, the effective Li ion diffusion coefficients are estimated from EIS,[27] according to the equation $D_{Li} = 1/2\{[V_m/(SF\sigma)][-(dE/dx)]\}^2$, where V_m is the mole volume of Si, S is the surface area of the electrode (estimated from the geometrical configuration of the nanocable electrode), F is the Faraday constant, σ is the Warburg factor which can be obtained from the fitting at low frequency in EIS, and dE/dx

can be estimated from the slope of galvanostatic charge−discharge profiles. The results of σ, dE/dx, and D_{Li} are summarized in Table S1 (Supporting Information). The effective Li-ion diffusion coefficient of the doped nanocable electrode is three times larger than that of the undoped nanocable electrode. It has been reported that the n-type doping for Si can decrease the energy barrier of Li surface intercalation, making the rate of Li transport increase to compare with the undoped sample.[12,14] Therefore, the improved effective Li-ion diffusion coefficient as well as the decreased lithiation voltage (inset of Figure 4a and 4b) of the N-doped nanocable electrode likely result from the decrease of the energy barrier of Li surface intercalation, leading to its better rate capabilities when compared to that of the undoped nanocable sample.

To further understand the cycling stabilities of the three electrodes, the morphological changes of the three electrodes were characterized at the delithiated state after the 30th cycle of the electrochemical test. Before the disassembling, the cells were held at 2 V vs Li^+/Li for 20 h to extract Li from Si as much as possible. Figure 5d−5f shows the morphologies of the sample pristine-TF30 min, sample pristine-NC30 min, and sample 0.5% N_2-NC30 min at the delithiated state (the SEI layer was already removed by dilute acetic acid). After cycling, the originally intact Si thin film breaks up into patches separated by interconnected cracks (Figure 5d). Although these patches of thin film fragments are not connected to each other, most of the pieces adhere to the substrate without delamination. For the sample pristine-NC30 min, the nanocable arrays fuse together after cycling (Figure 5e). In contrast, the well-separated nanocable array configuration is largely preserved in the sample 0.5% N_2-NC30 min (Figure 5f). It is known that Si suffers from large volume changes during the discharging/charging process, which can produce severe stress and even pulverize the Si anode.[28,29] Using nanocable arrays electrodes can alleviate the volume changes during cycling due to the porous nature of the electrode, leading to stress release. Nevertheless, in the presence of the same nanocable configuration, the morphology changes of the sample pristine-NC30 min and sample 0.5%-NC30 min are quite different after cycling (Figure 5e and 5f). As discussed before, the dopants can change the properties of Si in processes such as Li surface insertion[12,14] or electrochemical etching[30] or charge transfer in the electrode/electrolyte interface.[31] From this point of view, the processes of the SEI passivating layer formation on the active material surface are likely different in the doped and undoped Si. For example, the SEI passivating layer consists of a more stable LiF layer on the interface as has been observed in the n-doped Si electrode.[11] That probably explains the better preserved nanocable configuration of the sample 0.5% N_2-NC30 min after the cycling (Figure 5f). On the other hand, a fresh Si surface is exposed to electrolyte during the volumetric expansion to encourage continual growth of the SEI layer, resulting in continual irreversible capacity loss of the Si electrodes.[32] The formation of a more stable SEI layer in the N-doped nanocable sample consequently leads to its better cycling performance when compared to that of the undoped Si nanocable electrode (Figure 4d). A detailed understanding of the possible interfacial reactions and the SEI layer formation requires more work and is currently under investigation.

CONCLUSION

In summary, the effects of N doping on the electrochemical performance of Ni core/sputtered Si shell nanocable arrays were investigated as a LIB anode. In this composite electrode, not only the rate capabilities but also the cycling stabilities are improved through N doping. On the one hand, the interfacial resistance is reduced due to the improved electrical conductivity of Si upon doping. On the other hand, the effective Li ion diffusion coefficient of the doped nanocable array electrode is increased due to the decreased energy barrier of Li surface intercalation. Those features make the rate capabilities of the doped nanocable array electrodes increased. Moreover, a more stable SEI passivating layer is likely formed on the surface of the N-doped nanocable array electrode, resulting in its better cycling stability.

ASSOCIATED CONTENT

Supporting Information

R_{ohm}, R_{int}, σ, $|dE/dx|$, and D_{Li} of the Ni/Si nanocable array electrodes. R_{ohm} and R_{int} of the Si thin film electrode are also given. This material is available free of charge via the Internet at http://pubs.acs.org.

AUTHOR INFORMATION

Corresponding Author

*E-mail: liquan@phy.cuhk.edu.hk. Fax: +852 39435204. Tel.: +852 39436323.

Notes

The authors declare no competing financial interest.

ACKNOWLEDGMENTS

We acknowledge the support of General Research funding of the Research Grants Council of Hong Kong (No. 414612).

REFERENCES

(1) Cui, L.; Hu, L.; Wu, H.; Choi, J. W.; Cui, Y. *J. Electrochem. Soc.* **2011**, *158*, A592.
(2) Ohara, S.; Suzuki, J.; Sekine, K.; Takamura, T. *J. Power Sources* **2004**, *136*, 303−306.
(3) Yu, C.; Li, X.; Ma, T.; Rong, J.; Zhang, R.; Shaffer, J.; An, Y.; Liu, Q.; Wei, B.; Jiang, H. *Adv. Energy Mater.* **2012**, *2*, 68−73.
(4) Chan, C. K.; Peng, H.; Liu, G.; McIlwrath, K.; Zhang, X. F.; Huggins, R. A.; Cui, Y. *Nat. Nanotechnol.* **2008**, *3*, 31−5.
(5) Cui, L.; Ruffo, R.; Chan, C. K.; Peng, H.; Cui, Y. *Nano Lett.* **2008**, *9*, 491−495.
(6) Song, T.; Xia, J.; Lee, J. H.; Lee, D. H.; Kwon, M. S.; Choi, J. M.; Wu, J.; Doo, S. K.; Chang, H.; Park, W. I.; Zang, D. S.; Kim, H.; Huang, Y.; Hwang, K. C.; Rogers, J. A.; Paik, U. *Nano Lett.* **2010**, *10*, 1710−6.
(7) Wu, H.; Chan, G.; Choi, J. W.; Ryu, I.; Yao, Y.; McDowell, M. T.; Lee, S. W.; Jackson, A.; Yang, Y.; Hu, L. *Nat. Nanotechnol.* **2012**, *7*, 310−315.
(8) Saint, J.; Morcrette, M.; Larcher, D.; Laffont, L.; Beattie, S.; Pérès, J. P.; Talaga, D.; Couzi, M.; Tarascon, J. M. *Adv. Funct. Mater.* **2007**, *17*, 1765−1774.
(9) Cui, L. F.; Yang, Y.; Hsu, C. M.; Cui, Y. *Nano Lett.* **2009**, *9*, 3370−3374.
(10) Kim, J. W.; Ryu, J. H.; Lee, K. T.; Oh, S. M. *J. Power Sources* **2005**, *147*, 227−233.
(11) Andreas Arie, A.; Chang, W.; Kee Lee, J. *J. Electroceram.* **2010**, *24*, 308−312.
(12) Long, B. R.; Chan, M. K. Y.; Greeley, J. P.; Gewirth, A. A. *J. Phys. Chem. C* **2011**, *115*, 18916−18921.
(13) Masuda, A.; Itoh, K.-i.; Matsuda, K.; Yonezawa, Y.; Kumeda, M.; Shimizu, T. *J. Appl. Phys.* **1997**, *81*, 6729−6737.

(14) Peng, B.; Cheng, F.; Tao, Z.; Chen, J. *J. Chem. Phys.* **2010**, *133*, 034701−5.
(15) Ge, M.; Rong, J.; Fang, X.; Zhou, C. *Nano Lett.* **2012**, *12*, 2318−2323.
(16) Nelson, G. J.; Cassenti, B. N.; Peracchio, A. A.; Chiu, W. K. S. *J. Electrochem. Soc.* **2012**, *159*, A598−A603.
(17) Kim, J. B.; Jun, B. S.; Lee, S. M. *Electrochim. Acta* **2005**, *50*, 3390−3394.
(18) Liu, H.; Hu, L.; Shirley Meng, Y.; Li, Q. *Nanoscale* **2013**, *5*, 10376−10383.
(19) Choi, J. W.; McDonough, J.; Jeong, S.; Yoo, J. S.; Chan, C. K.; Cui, Y. *Nano Lett.* **2010**, *10*, 1409−1413.
(20) Karunasiri, R. P. U.; Bruinsma, R.; Rudnick, J. *Phys. Rev. Lett.* **1989**, *62*, 788−791.
(21) Hatchard, T.; Dahn, J. *J. Electrochem. Soc.* **2004**, *151*, A838−A842.
(22) Chen, X.; Gerasopoulos, K.; Guo, J.; Brown, A.; Wang, C.; Ghodssi, R.; Culver, J. N. *ACS Nano* **2010**, *4*, 5366−5372.
(23) Mahmood, N.; Zhang, C.; Hou, Y. *Small* **2013**, *9*, 1321−1328.
(24) Mahmood, N.; Zhang, C.; Jiang, J.; Liu, F.; Hou, Y. *Chem.—Eur. J.* **2013**, *19*, 5183−5190.
(25) Ruffo, R.; Hong, S. S.; Chan, C. K.; Huggins, R. A.; Cui, Y. *J. Phys. Chem. C* **2009**, *113*, 11390−11398.
(26) Arthur, T. S.; Bates, D. J.; Cirigliano, N.; Johnson, D. C.; Malati, P.; Mosby, J. M.; Perre, E.; Rawls, M. T.; Prieto, A. L.; Dunn, B. *MRS Bull.* **2011**, *36*, 523−531.
(27) Ho, C.; Raistrick, I.; Huggins, R. *J. Electrochem. Soc.* **1980**, *127*, 343−350.
(28) Li, J. C.; Dozier, A. K.; Li, Y. C.; Yang, F. Q.; Cheng, Y. T. *J. Electrochem. Soc.* **2011**, *158*, A689−A694.
(29) Soni, S. K.; Sheldon, B. W.; Xiao, X. C.; Tokranov, A. *Scr. Mater.* **2011**, *64*, 307−310.
(30) Eddowes, M. J. *J. Electroanal. Chem. Interfacial Electrochem.* **1990**, *280*, 297−311.
(31) Kim, J. S.; Choi, W.; Byun, D.; Lee, J. K. *Solid State Ionics* **2012**, *212*, 43−46.
(32) Szczech, J. R.; Jin, S. *Energy Environ. Sci.* **2011**, *4*, 56−72.